EES Batteries

PAPER

View Article Online
View Journal

Cite this: DOI: 10.1039/d6eb00095a

Intergranular degradation of secondary NMC particles in liquid and solid-state environments

Fernando D. Cúñez, *[a,d] Radwa Elawadly,[a] Eric Hintsala,[b] Wonjoon Suk,[c] Yiyang Li *[c] and Qingsong Howard Tu *[a]

The growing demand for high-performance and reliable energy storage systems is driving advancements in cathode optimization in lithium-ion battery technologies. This study investigates particle-scale intergranular mechanical degradation of secondary NMC particles in both liquid and solid-state environments, highlighting the critical role of microstructural evolution, electrolyte medium, and fabrication conditions in influencing different cathode environments. Single-particle electrochemical cycling experiments, single-particle SEM-nanoindentation tests, and continuum modeling were employed to investigate how different cycling conditions impact mechanical integrity and fracture behavior. Computational Fluid Dynamics (CFD) and Discrete Element Method (DEM) were employed to numerically assess the mechanical degradation of secondary NMC particles under electrochemical cycling in liquid electrolyte and solid electrolyte environments. Our findings on liquid environments pinpoint the first charge as the critical point of mechanical failure with a complex and non-linear degradation pathway. The particle fracture strength (σ_T) degrades dramatically from a pristine value of ~220 MPa to ~50 MPa (about 80%) after the first charge. This is followed by a significant mechanical recovery after the first discharge, where the strength is partially restored to ~100 MPa. After the first cycle, the particle strength continues to decrease more gradually, reaching about 90 MPa after 10 cycles. Conversely, solid-contact environments demonstrate much better mechanical stability. Despite a lower fracture strength of ~102 MPa compared to liquid environments after the first cycle, they show a much slower decay, retaining a strength of approximately 95 MPa after 10 cycles. It was also revealed that a composite cathode made with excessive fabrication pressures above 500 MPa may cause secondary NMC particle fragmentation, leading to reduced ionic conductivity and capacity retention. Overall, this work provides a particle-resolved mechanical framework—supported by simulations—for interpreting and mitigating intergranular degradation in secondary NMC across liquid and solid-state environments.

Received 29th April 2026,
Accepted 1st May 2026

DOI: 10.1039/d6eb00095a

rsc.li/EESBatteries

Broader context

The global push for sustainable energy hinges on advancing energy storage technologies. While conventional lithium-ion batteries, which utilize liquid electrolytes, have been transformative, there is a pressing need to enhance their durability and lifespan. Concurrently, the development of solid-state batteries represents a critical next step toward next-generation energy storage, promising significant improvements in safety and energy density. A pivotal challenge hindering progress in both of these distinct battery architectures is the mechanical degradation of cathode materials. This research directly addresses this issue by providing a fundamental comparison of the failure mechanisms of NMC532 and NMC811 in both liquid and solid-state environments. Our findings reveal divergent degradation pathways: a critical fracture point during the initial charge in liquid-based systems, contrasted with a sensitivity to manufacturing pressures in their solid-state counterparts. This nuanced understanding is essential for engineering more resilient cathode microstructures and optimizing manufacturing protocols for both current and future battery technologies, thereby accelerating the transition to a more sustainable energy landscape.

[a]Department of Mechanical Engineering, Rochester Institute of Technology, Rochester, 14623 NY, USA. E-mail: fcunezbe@ur.rochester.edu, howard.tu@rit.edu
[b]Bruker Nano Surfaces & Metrology, 9625 West 76th St, Eden Prairie, 55344 MN, USA
[c]Materials Science and Engineering, University of Michigan, Ann Arbor, 48109 MI, USA. E-mail: yiyangli@umich.edu
[d]Department of Earth and Environmental Sciences, University of Rochester, Rochester, 14627 NY, USA

1 Introduction

Advancing the performance and durability of batteries is essential to meet the growing global demand for reliable and efficient energy storage systems,[1–3] which are critical for applications such as electric vehicles, portable electronics, and renewable energy integration.[4–6] While lithium-ion batteries

remain the dominant technology, the pursuit of higher energy density, improved safety, and enhanced cycling stability has accelerated the development of all-solid-state batteries (ASSBs) as a promising alternative.[7,8] A key innovation in ASSBs is the use of composite cathodes, comprising a mixture of cathode active materials (CAMs), solid electrolytes (SEs), and conductive additives, which offer the potential for increased energy densities.[9–11] However, the transition from liquid to solid electrolytes introduces new mechanical challenges. The mismatch in elastic properties between CAMs and SEs particles leads to stress accumulation at interfaces, promoting crack initiation and propagation that compromise mechanical integrity and battery performance.[12–15] Similarly, in liquid electrolyte systems, fluid-induced stresses can accelerate degradation by infiltrating microcracks and weakening grain boundaries.

Among the cathode active materials, nickel-rich layered oxides, such as $LiNi_xMn_yCo_zO_2$ (NMC), have emerged as a primary choice to assemble cathodes due to their high specific capacity and energy density.[16–18] However, the volumetric expansion and contraction that NMC particles experience during cycling represent significant mechanical challenges, resulting in issues such as the concentration of gradients and the loss of contact that lead to poor ionic transport and capacity loss.[19–21] NMC particles are often found in two configurations depending on their size: primary particles, which commonly display diameters lower than 5 μm, and secondary particles, also known as polycrystalline particles, which are clusters of smaller primary particles, exhibiting larger diameters (≈10 μm).[13,17,22]

In lithium-ion batteries, the use of secondary NMC particles has been widely adopted to achieve higher energy densities and excellent electrochemical performance.[23–25] However, their polycrystalline nature introduces numerous grain boundaries, which act as potential sites for intergranular mechanical degradation during electrochemical cycling. Interestingly, while intergranular degradation is often perceived as detrimental, recent studies suggest that it can play a nuanced role in mechanical and electrochemical stability. For instance, intergranular cracks may improve electrolyte penetration, enhancing reaction kinetics and reducing diffusion limitations within the particle, as demonstrated in recent single-particle electrochemical studies.[17] An additional challenge arises with nickel-rich NMC compositions, which, while offering higher energy densities, often suffer from reduced safety and shorter cycle life. The aging and degradation of these materials can follow several pathways, including microcracking, undesired phase transitions, and transition metal (TM) dissolution. TM dissolution not only weakens the cathode structure but also contributes to the degradation of the anodic solid-electrolyte interphase (SEI) and the loss of lithium inventory, further accelerating capacity fade and reducing cycling stability.[26–30]

In all solid-state batteries, secondary particles have been commonly used since they offer a wider range in size, allowing cathodes to have higher cathode active materials loading with high utilization when they are larger than SE particles.[10,31] One of the primary issues of using secondary NMC particles is their susceptibility to mechanical degradation. During electrochemical cycling, the repeated insertion and extraction of lithium ions induce diffusion-induced stress (DIS), leading to the formation of cracks.[12,14,15,21,22,32,33] These cracks propagate through both intergranular and intragranular pathways, reducing electrical contact, increasing interfacial resistance, and ultimately degrading battery performance.[14,17,34] The polycrystalline nature of secondary particles leads to the formation of multiple grain boundaries, which act as weak points that are prone to intergranular cracking, having a more immediate and severe impact on ASSBs, requiring less energy than intragranular cracking.[22]

Prior work on NMC811/Li_6PS_5Cl solid-state batteries has extensively examined post-cycling interfacial chemistry and degradation using complementary characterization methods. Surface-sensitive spectroscopy (*e.g.*, XPS and XAS) has been used to track changes in transition-metal oxidation states and identify sulfide-electrolyte decomposition products, while high-resolution microscopy and microanalysis (*e.g.*, STEM-EDX and EELS) have resolved interfacial reaction layers and mapped elemental distributions after cycling.[35–37] These studies consistently show that interfacial side reactions and interphase formation occur in NMC/Li_6PS_5Cl composite cathodes.

Several approaches have been explored to understand and address these degradation mechanisms. For instance, recent studies have investigated the role of the microstructure in both rate performance and defect heterogeneities in single-crystal and secondary NMC particles, where the capacity-rate performance can be enhanced by decreasing the secondary particle size; meanwhile, the operating conditions and the random distribution of primary particles in the secondary particle play a crucial role in the stress concentrations due to dislocation heterogeneity.[13,17] While intergranular cracking in polycrystalline NMC and pressure-dependent performance trends in sulfide-based composite cathodes have been reported in prior studies,[12,17] important gaps remain in quantitatively linking electrochemical state to particle-scale mechanical integrity and in separating how environmental boundary conditions (liquid exposure *versus* solid-contact confinement) shape damage evolution.

In this work, we investigate how particle microstructure, electrochemical environment, and processing constraints govern intergranular mechanical degradation in polycrystalline secondary NMC. Using single-particle electrochemical cycling coupled with post-cycling SEM–nanoindentation fracture measurements on NMC532 and NMC811, we quantify cycling-state-dependent changes in particle fracture behavior. We complement these experiments with DEM and CFD–DEM simulations to resolve grain-scale stress redistribution, intergranular cohesion loss, and crack/fragmentation evolution under liquid electrolyte exposure and solid-contact confinement. In parallel, we evaluate how fabrication pressure impacts microstructural evolution within Li_6PS_5Cl-based composite cathodes, linking pressure-driven fragmentation/contact changes to electrochemical outcomes (capacity retention and impedance evolution). Because all solid-state cells were pre-

pared using the same materials (including the same Li_6PS_5Cl batch), identical cathode formulations, and the same electrochemical protocol—varying only fabrication pressure—the pressure-dependent trends were interpreted primarily through pressure-modulated microstructural and mechanical changes (fragmentation, contact evolution, and effective transport pathways), while recognizing that interfacial chemistry may co-exist and contribute to baseline degradation.

2 Methods

2.1 Materials and sample preparation of single polycrystalline NMC particles for the electrochemical test

The experimental setup employed a microfabricated microelectrode array, similar to that described in Min *et al.*[17] and Suk *et al.*[38] The microchip platform used in this study was adapted from previous designs. The microelectrode array consisted of a 3 × 3 cm silicon chip with a 500 nm thermal oxide layer. Microelectrodes were patterned using photolithography and electron beam evaporation, depositing 5 nm Ti and 100 nm Au layers. The array contained 200 square gold (Au) microelectrodes and one large Au counter electrode, all patterned on a silicon wafer. The working electrodes were electrically connected to contact pads using 20 μm patterned Au wires and passivated with a 50 nm SiN layer to prevent parasitic reactions, leaving only the electrode tips exposed for the electrochemical interaction.

For the particle assembly, 16 polycrystalline NMC532 and 16 polycrystalline NMC811 particles with diameters ranging between 7 and 11 μm were positioned on the microelectrodes using a 1 μm tungsten needle mounted on an XYZ micromanipulator. Each particle was positioned onto an exposed Au contact, ensuring direct electronic connection for accurate electrochemical measurements. The particles were uniformly distributed to avoid overlap and ensure independent electrochemical cycling. Particle morphology and size were characterized *via* scanning electron microscopy (SEM) prior to electrochemical cycling. Post-cycling analyses included capacity measurements.

The counter electrode consisted of partially delithiated $Li_{0.6}FePO_4$, mixed with polyvinylidene fluoride (PVDF) and carbon black in a 7 : 2 : 1 weight ratio. The slurry was placed onto the counter electrode pad and dried at 80 °C to ensure solvent evaporation. A 1 M $LiPF_6$ solution in propylene carbonate (PC) was used as the electrolyte, with 3 μL drop-cast onto the microchip to cover the electrodes and ensure ionic connectivity. A stainless steel cap was placed over the chip to minimize electrolyte evaporation. The electrochemical experiments were conducted under four distinct conditions to investigate particle behavior under different stress scenarios:

1. Pristine particles without cycling but after immersion in the electrolyte (4 particles for each type of NMC).

2. Single charge cycle: particles were charged once to a cutoff voltage of 4.25 V at a C-rate of C/3 (4 particles for each type of NMC).

3. Single charge–discharge cycle: particles were charged to 4.25 V and then discharged to 2.5 V (4 particles for each type of NMC).

4. 10 charge/discharge cycles between 2.5 and 4.25 V, ending at 2.5 V (4 particles for each type of NMC).

All single-particle electrochemical tests were performed using a Bio-Logic VMP300 potentiostat under an argon-filled glove box to minimize contamination and oxidation. Single-particle cycling was conducted at C/3 as a baseline rate that balances reduced polarization/gradient effects with experimental throughput, enabling reproducible testing across multiple particles and electrochemical states.

2.2 Mechanical characterization of single NMC particles

The mechanical properties of the secondary NMC particles were assessed using a Hysitron PI-89 PicoIndenter from Bruker (https://www.bruker.com), a transducer able to measure a maximum force of 500 mN, a B-doped diamond 20 μm flat punch, operating inside a Versa3D Focused Ion Beam Scanning Electron Microscope (FIBSEM) from Thermo Fisher (https://www.thermofisher.com). The loading was displacement-controlled at a rate of 40 nm s^{-1} and the tests were stopped upon particle fracture. The Hiramatsu and Oka model[39,40] was then used to estimate the fracture stress as follows: $\sigma_T = (\kappa F_c)/(\pi R^2)$, where F_c is the fracture force measured in the nanoindentation experiment, R is the particle radius, and κ is a constant here set to 0.7 (see SI section I for a detailed explanation of the model).

2.3 Solid-state battery cell assembling procedure and electrochemical characterization

To investigate the mechanical and electrochemical performance of secondary NMC532 and NMC811 particles in solid-state battery environments, we fabricated full solid-state battery cells using Li_6PS_5Cl (LPSCL) as the solid electrolyte and NMC532 and NMC811 as the cathode active material. Lithium metal pellets were used as the anode. All sample preparation and mixing were carried out in an argon-filled glovebox, maintaining oxygen levels below 1 ppm to prevent contamination and degradation of the solid electrolyte and electrode materials. The cell assembly was performed within a polyether ether ketone (PEEK) tube with an inner diameter of 6.35 mm, ensuring a well-confined structure for mechanical and electrochemical testing.

The composite cathode was prepared by manually blending 48 wt% NMC532 or NMC811, 48 wt% LPSCL, and 4 wt% carbon nanofiber for 15 minutes using a mortar and pestle, ensuring uniform distribution of the active material, solid electrolyte, and conductive additive. To study the effect of fabrication pressure on mechanical and electrochemical stability, the cathode was compacted at three different pressures: 300 MPa, 500 MPa, and 700 MPa. The solid electrolyte/separator was constructed using 45 mg of LPSCL powder, positioned between the cathode and the lithium metal anode. The final full-cell assembly was completed by applying the designated

pressure using a cold press, compacting the full cell into a dense structure within the PEEK tube.

Electrochemical characterization was performed using a 6-channel potentiostat (Bio-Logic VMP300 system, France). Capacity measurements were conducted at room temperature, with voltage cycling between 2.5 V and a cut-off voltage of 4.25 V, applying a constant current of 0.16 mA. This setup allowed for direct evaluation of how fabrication pressure influences electrochemical performance, cycling stability, and capacity retention in solid-state battery configurations.

2.4 Model description

In our numerical simulations, we used the open-source code LIGGGHTS[41] to compute the solid–solid interactions of primary particles by solving the linear and angular Newton's second law. For particle–particle and particle–wall contacts, the Hertzian granular contact model is used to describe normal and tangential interactions and damping forces, as well as frictional yield, as shown in the following expression:

$$F = (k_n \delta n_{ij} - \gamma_n \nu n_{ij}) + (k_t \delta t_{ij} - \gamma_t \nu t_{ij}) \quad (1)$$

where the first and second terms are the normal and tangential force between the two particles, respectively: each term being the spring ($k_x \delta x_{ij}$) and the damping force ($\gamma_x \nu x_{ij}$) in the Hertzian model (see SI section II for a detailed explanation of the DEM model). To numerically obtain the aggregated secondary NMC particle, we also used the simplified Johnson–Kendall–Roberts (SJKR) cohesion model that adds an additional normal force that tends to maintain the contact between particles following the expression $F_{\text{cohe}} = kA$, where A is the particle contact area and k is the cohesion energy density. Since there is no available data on the cohesion energy density of secondary NMC particles in the literature, we iteratively calculated k based on the bulk modulus obtained from pristine secondary NMCs. Material properties of NMC particles used in the numerical simulations such as Young's modulus, Poisson's ratio, coefficient of restitution and coefficient of friction were obtained from previous studies[42] and are detailed in the SI. Fig. 3 illustrates the DEM model used to simulate the mechanical behavior of pristine secondary particles under compression, along with the experimental validation of the model.

Finally, the mechanical behavior of secondary NMC particles during electrochemical cycling was modeled by controlling the volumetric changes of the primary grains to replicate the effects of lithiation and delithiation. Each secondary particle was constructed as an aggregate of spherical primary particles, and their expansion and contraction behavior was systematically controlled to mimic the volumetric fluctuations induced by lithium insertion and extraction. Specifically, the primary spheres were programmed to isotropically expand and contract up to 10% of their initial volume, reflecting the typical volume change of NMC materials during cycling.

On the other hand, to evaluate the impact of fluid flow on the mechanical degradation of secondary NMC particles in liquid-electrolyte environments, coupled CFD-DEM simulations were conducted using the open-source code CFDEM (https://www.cfdem.com).[41] This approach enabled the detailed investigation of particle–fluid interactions and how electrolyte flow dynamics influence mechanical stress accumulation and crack propagation within secondary particles. The simulations were performed using the immersed boundary method (IBM) integrated with a CFD-DEM framework. The CFD solver addressed fluid dynamics within interstitial spaces of secondary particles, while the DEM solver tracked the motion and interaction of individual primary grains. This fully resolved approach allowed the simultaneous evaluation of fluid forces acting on particles and mechanical interactions between grains.

3 Results

3.1 Single-particle electrochemical cycling

Fig. 1 illustrates the experimental setup and electrochemical cycling behavior of secondary NMC particles. Fig. 1a presents the microelectrode array chip used for single-particle electrochemical cycling. The chip consists of an array of 60 working microelectrodes fabricated to enable the precise placement and cycling of individual particles. Fig. 1b shows the optical and scanning electron microscopy images of a particle placed on the microelectrode prior to electrochemical cycling and nanoindentation experiments (see SI sections III and IV for SEM images of each tested particle). This particle isolation on individual microelectrodes ensures that the measured electrochemistry contains information from a single NMC cathode particle.

Fig. 1c–e display electrochemical cycling for three separate particles placed on different microelectrodes. The first particle underwent just a single charge cycle to 4.25 V at a rate of C/3. The second particle underwent one charge and a discharge cycle. The third particle underwent 10 charge and discharge cycles (other electrochemical cycling data are included in the SI). Nanoindentation experiments were performed on 24 cycled particles as well as 8 pristine uncycled particles.

3.2 Mechanical degradation analysis *via* nanoindentation

The mechanical degradation behavior of secondary particles within NMC during electrochemical cycling reveals the complex interplay between internal stress evolution and microstructural changes. As shown through nanoindentation experiments (Fig. 2), the degradation process is neither linear nor uniform but is influenced by the cycling stage and the resulting microstructural transformations.

Initial observations of pristine particles reveal a robust and high mechanical integrity, exhibiting a high fracture stress of ~220 MPa (Fig. 2a). However, this stability is quickly compromised after just one charging cycle to 4.25 V, where the fracture stress shows a drastic decay to ~50 MPa (Fig. 2b). Since charging involves lithium extraction (delithiation) from the NMC particles, the resulting decrease in lithium content trig-

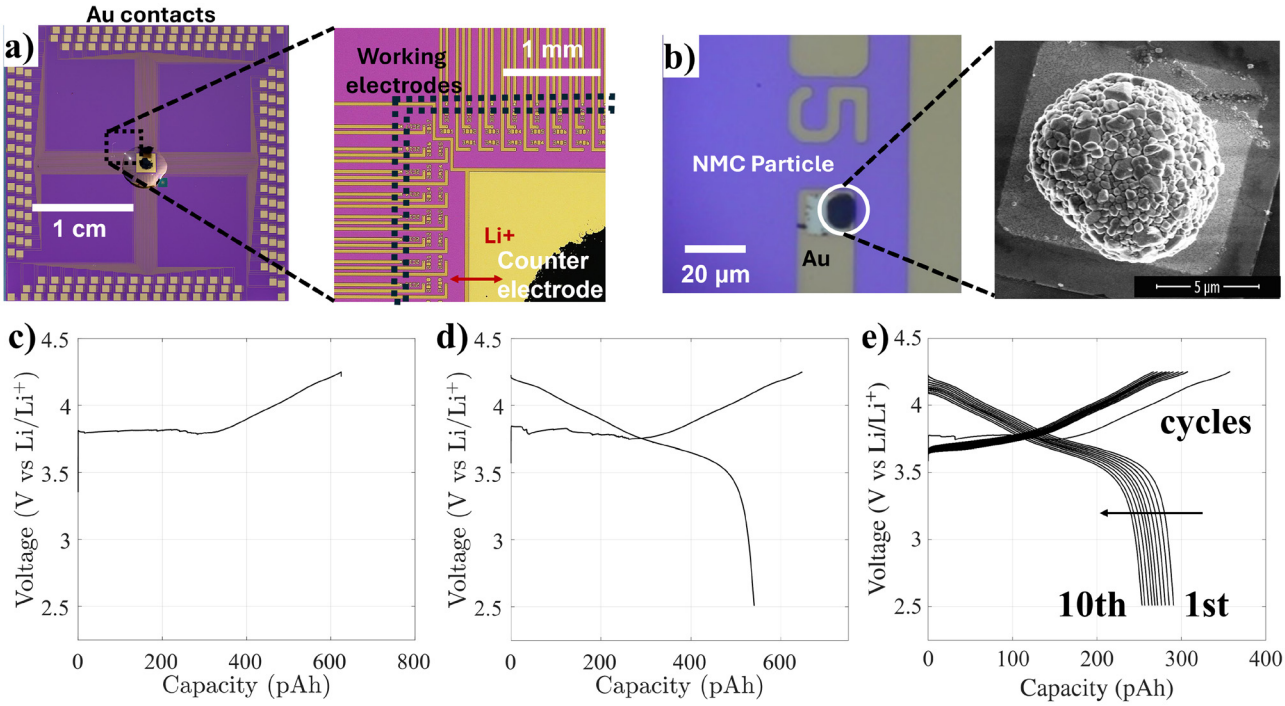

Fig. 1 Single-particle electrochemistry of polycrystalline cathode particles. (a) Schematic and image of the microelectrode array used for single-particle electrochemistry. (b) Optical and scanning electron micrograph of a particle prior to electrochemical cycling. (c–e) Single-particle electrochemical cycling of a particle undergoing 1 charge cycle, 1 charge and discharge cycle, and 10 charge/discharge cycles.

gers a lattice contraction. This contraction induces internal stress, particularly along grain boundaries, promoting the initiation of microcracks and surface degradation.

Interestingly, after completing a full charge–discharge cycle, the mechanical integrity of the secondary particle exhibits partial recovery, showing fracture stresses of ~100 MPa (Fig. 2c). During discharge, lithium reinsertion (lithiation) into the NMC lattice leads to volumetric expansion, which may help alleviate some internal stresses and reduce the severity of microcrack propagation. The restored lattice structure appears to temporarily re-establish mechanical stability, making the surface more compact compared to the solely charged state. However, this mitigation is only partial, as irreversible microstructural damage accumulates over successive cycles, where after 10 cycles, fracture stress degrades further to ~90 MPa, highlighting that repetitive cycling leads to cumulative mechanical fatigue and crack evolution.

The development of deep intergranular cracks reflects the cumulative fatigue experienced by the particle, resulting from repetitive lithiation–delithiation-induced stress fluctuations. This progressive deterioration aligns with the fracture stress evolution trends. Fracture stress drops sharply after the initial charge, suggesting rapid mechanical weakening, which partially recovers after discharge, but ultimately declines after prolonged cycling. This trend underscores the critical influence of cycling dynamics on mechanical stability. The sharp initial degradation suggests that lithium insertion imposes significant mechanical stress, while subsequent discharge offers only a temporary reprieve. Ultimately, extended cycling results in accumulated mechanical fatigue, leading to structural collapse (see SI sections III and IV for load *vs.* displacement curves for each tested particle).

The DEM simulations, represented by the magenta squares in Fig. 2e and magenta stars in Fig. 2f, closely align with the experimental results, validating the simulation framework and confirming that the surface energy parameters derived from experiments accurately capture mechanical degradation trends.

3.3 Correlation between mechanical degradation and electrochemical cycling

Fig. 2f shows the evolution of the fracture stresses and specific capacity (Inset) across different cycling stages. Capacities measured in pAh were converted to gravimetric units (mAh g^{-1}) by determining particle volume *via* SEM-based image analysis, calculating particle mass from the estimated volume and density, and normalizing capacity accordingly. The relationship between capacity and fracture strength is not linear; instead, it highlights the trade-offs of the electrochemical processes. For the pristine conditions, we consider a theoretical capacity of 240 mAh g^{-1} for the case of NMC811 and 200 mAh g^{-1} for the case of NMC532 based on the previous work.[43]

After the first charge, the battery achieves its maximum experimental capacity (~240 mAh g^{-1} for NMC811 and ~200 mAh g^{-1} for NMC532), but the particles experience their most severe drop in mechanical strength (from ~220 MPa to

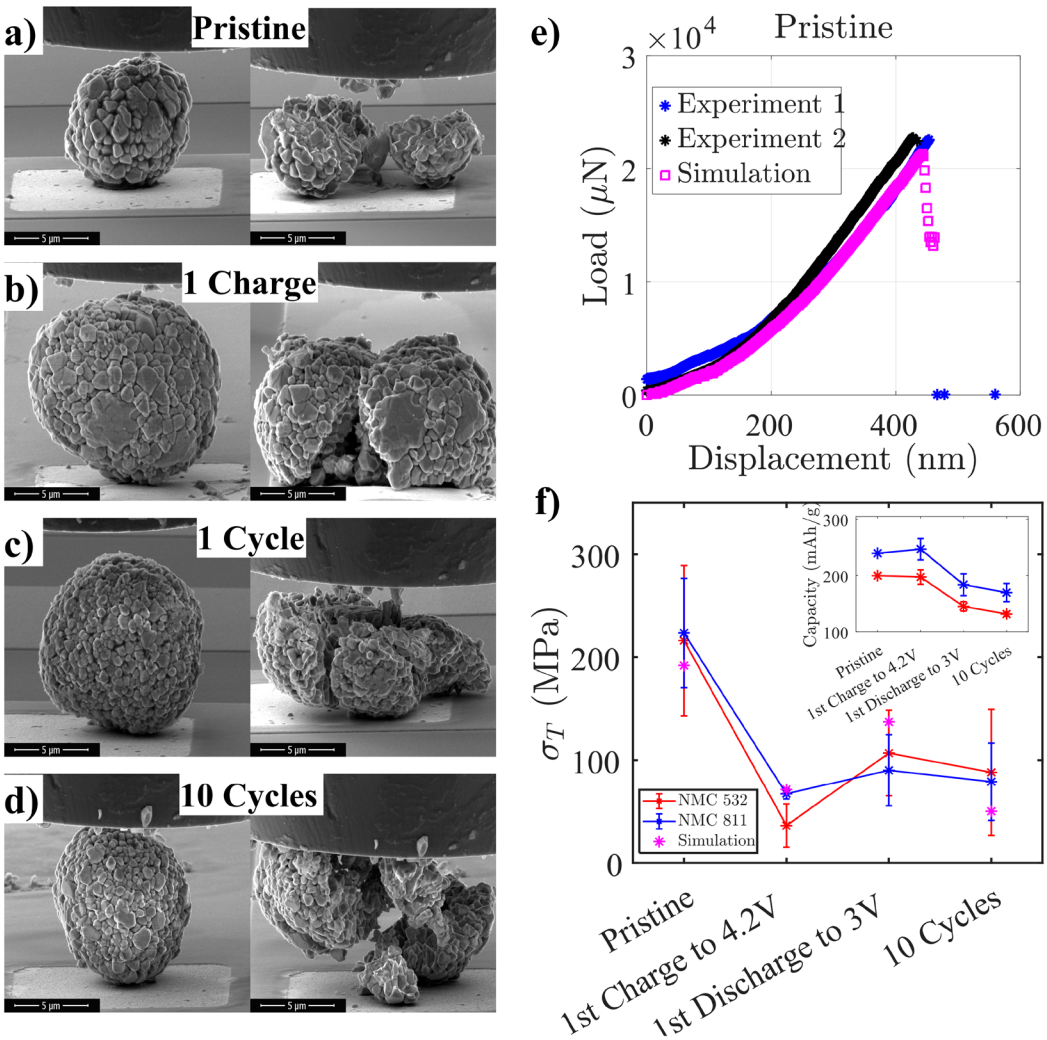

Fig. 2 Nanoindentation experiments in pristine secondary NMC particles: (a–d) SEM images before and after compression testing in a secondary particle with a diameter of 8 μm; (a) pristine NMC (no cycling); (b) NMC after 1 charge; (c) NMC after 1 charge and discharge; (d) NMC after 10 cycles; (e) load *vs.* displacement curves obtained from both nanoindentation experiments and simulations; and (f) fracture stresses obtained from the nanoindentation experiments for both NMC532 and NMC811 and specific capacities under different electrochemical conditions (inset).

~50 MPa). This shows that the initial electrochemical activation is mechanically damaging. After the first full cycle, an interesting divergence occurs. While the capacity begins to fade, the particle strength actually recovers significantly (to ~100 MPa). This suggests that structural relaxation during discharge alleviates some of the mechanical stress introduced during charging. Finally, over the long term (by 10 cycles), the two trends align. The continued mechanical degradation, resulting in low fracture strength (~100 MPa) and visible particle cracking (Fig. 2d), is correlated with significant capacity loss. This is because fractured particles can become electrically isolated from the electrode, ceasing to contribute to the capacity.

3.4 NMC behaviors in liquid and solid environments

We systematically investigate the mechanical degradation of secondary NMC particles within both liquid and solid electrolyte environments, recognizing that the surrounding medium plays a critical role in influencing stress distribution, crack propagation, and overall particle stability. Understanding these differences is essential, as lithium-ion batteries (with liquid electrolytes) and all-solid-state batteries (with solid electrolytes) present distinct mechanical challenges. In liquid environments, the electrolyte can infiltrate microcracks and exacerbate degradation through continuous fluid-induced stresses, while in solid environments, the confinement imposed by solid electrolyte particles introduces localized stress concentrations, particularly during fabrication and cycling.

Our numerical model captures the complexity of secondary NMC structures by representing them as aggregates of spherical primary grains, with intergranular cohesion (represented in blue in Fig. 3c). This cohesive force framework is particularly novel, as it directly addresses the role of grain boundaries in

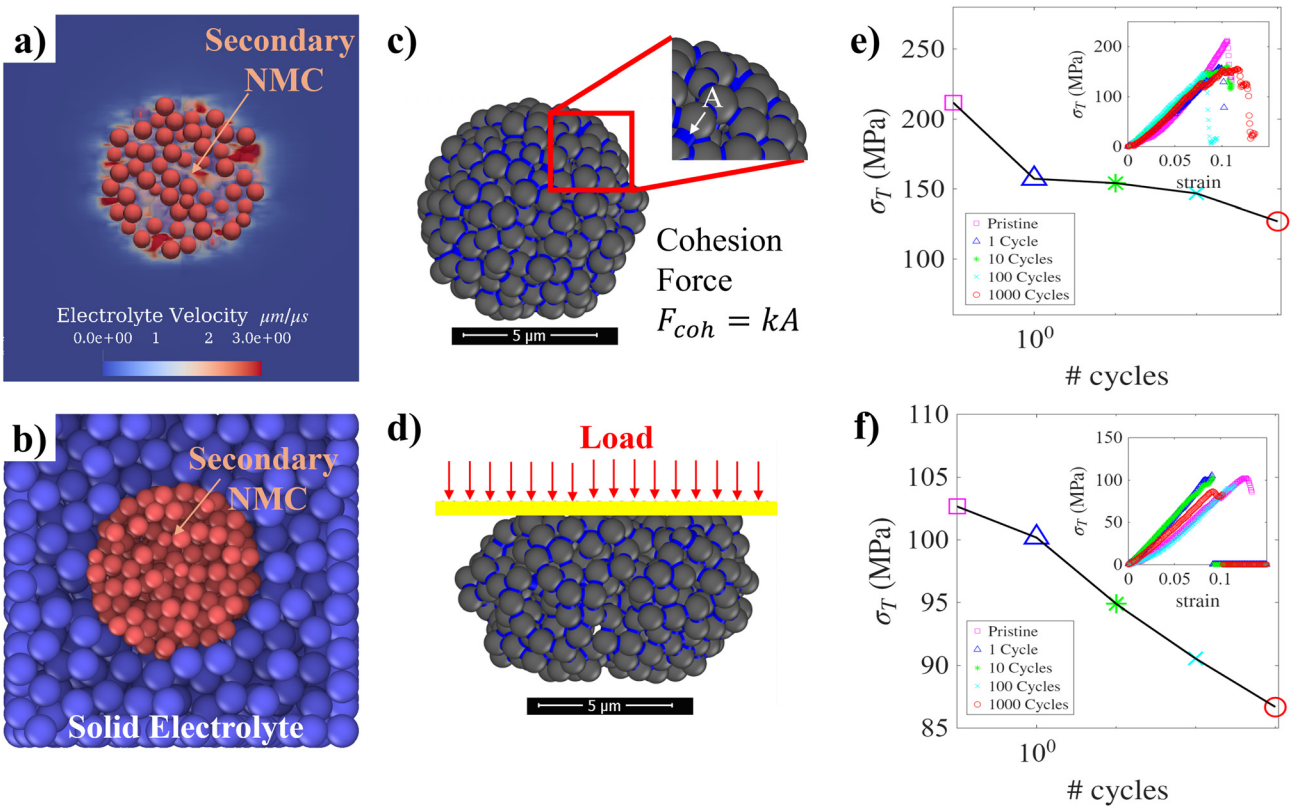

Fig. 3 Li-ion batteries *vs.* solid-state batteries: (a) CFD-DEM numerical simulation of a secondary NMC particle inside a liquid medium (color gradient indicates the electrolyte velocity surrounding the particle); (b) DEM numerical simulation of a secondary NMC particle within the solid electrolyte (SE); (c and d) diagram of DEM simulations after cycling to obtain fracture stresses in both environments; (e) fracture stress *vs.* the number of cycles of a secondary NMC particle inside a liquid medium after 1, 10, 100, and 1000 cycles; and (f) fracture stress *vs.* the number of cycles of a secondary NMC particle inside a solid medium after 1, 10, 100, and 1000 cycles.

mechanical stability (an aspect often overlooked in simpler continuum models). The simulation framework captures how these intergranular cohesive bonds respond to mechanical stress and how their failure initiates and propagates cracks within the secondary particle (Fig. 3d). This approach allows for an unprecedented level of detail in modeling microstructural interactions, providing insights into how intergranular forces influence overall mechanical resilience.

3.4.1 Liquid electrolyte environment (Li-ion batteries). The influence of the liquid electrolyte environment on the mechanical degradation of secondary NMC particles is complex, as revealed through CFD-DEM simulations (Fig. 3a and e). The simulations highlight that electrolyte flow is not a passive component but an active driver of mechanical stress within the particle structure. Fluid infiltrates the interstitial spaces of the polycrystalline particle, interacting with grain boundaries and exerting shear forces that accelerate crack initiation and propagation (Fig. 3a). This process is especially concerning because it introduces continuous stress cycles, even beyond the direct effects of lithiation and delithiation. The dynamic interaction between the fluid and the particle structure weakens cohesive bonds, creating pathways for microcracks to evolve and propagate deeper with each cycle. This insight emphasizes that the liquid medium is not merely a facilitator of ion transport but also a significant contributor to mechanical fatigue, gradually impacting the structural integrity of the particles.

The cumulative effects of cycling further highlight the aggressive nature of mechanical degradation in liquid environments. The stress–strain behavior of secondary NMC particles subjected to 1, 10, 100, and 1000 cycles (Fig. 3e) shows a clear, progressive decline in fracture stress, dropping from 220 MPa under pristine conditions to 120 MPa after 1000 cycles. This continuous degradation is not merely the result of electrochemical strain but is compounded by the persistent action of fluid-induced stresses. As microcracks form and propagate, the electrolyte infiltrates these pathways, exacerbating grain boundary weakening and reducing the particle's ability to withstand mechanical load. The simulations confirm that the liquid medium acts as a catalyst for mechanical fatigue, steadily eroding particle cohesion over extended cycling.

3.4.2 Solid electrolyte environment (ASSBs). The mechanical behavior of secondary NMC particles within a solid electrolyte (SE) environment presents a distinct set of challenges and degradation pathways, as revealed by the DEM simulations. Unlike liquid electrolytes, where fluid movement can exacer-

bate crack propagation, the solid matrix imposes a rigid, confining structure around the secondary NMC particles (Fig. 3b). While this confinement can stabilize the electrode to some extent, it also restricts particle expansion during lithiation, concentrating stress at particle boundaries. This localized stress accumulation becomes a critical factor in crack initiation and propagation, particularly as repeated cycling intensifies internal stresses. This interaction between particle expansion and confinement underscores the nuanced role of the solid medium not merely as a structural framework but as an active participant in mechanical degradation phenomena.

The evolution of fracture stress during cycling (Fig. 3f) emphasizes the complex relationship between mechanical degradation and electrochemical performance in solid-state systems. Although the degradation in fracture stress is less severe than in liquid environments, the gradual decline from 100 MPa to 86 MPa after 1000 cycles reflects the persistent influence of repeated volume changes. The solid electrolyte confines particle expansion, which mitigates some stress-induced cracking but cannot entirely eliminate mechanical fatigue. Over time, localized stress concentrations lead to microcrack formation, contributing to gradual mechanical degradation.

The fabrication pressure applied during the manufacturing of all-solid-state batteries (ASSBs) can also induce significant stress on secondary NMC particles, prompting a closer examination of its role in mechanical degradation. Fig. 4 shows the influence of the fabrication pressure on the overall performance in ASSBs. Fig. 4b presents the evolution of tortuosity and relative density as a function of the fabrication pressure to understand the mechanical integrity of secondary NMC particles. Initially, increasing fabrication pressure up to an optimal range of around 100–300 MPa promotes better particle packing and interconnectivity, reducing tortuosity and improving potential ion transport pathways. This indicates that the pressure effectively improves particle packing and densifies the composite cathode, creating more direct and efficient pathways for lithium-ion transport. However, beyond this point, increasing pressure leads to increased tortuosity. This reversal signifies that excessive pressure, particularly above 300 MPa, induces mechanical damage, causing the secondary NMC particles to fracture. These cracks create longer and convoluted pathways for ions, increasing tortuosity and impeding ionic conductivity.

This mechanical behavior directly correlates with the electrochemical performance shown in Fig. 4d–f. While the lowest tortuosity is achieved around 100–300 MPa, the highest discharge capacity after both 1 and 10 cycles is observed at 500 MPa (Fig. 4e and g). This suggests that while some minor particle cracking may begin above 300 MPa (as indicated by the rising tortuosity), the benefits of superior densification (about 88% of relative density at 500 MPa) and enhanced interfacial contact between the NMC active material and the solid electrolyte continue to improve performance up to 500 MPa. By 700 MPa (Fig. 4f and g), mechanical degradation becomes too severe; the extensive particle fracture and resulting high tortuosity significantly compromise ion transport pathways, leading to a noticeable drop in the discharge capacity (see SI section VII for Nyquist impedance plots of the 3 fabrication pressures). Therefore, 500 MPa represents the optimum fabrication pressure within the explored window in this study, successfully balancing the positive effects of densification against the negative impact of particle fracture to achieve the highest cell performance. These findings suggest that while densification is crucial for achieving optimal initial contact, over-compaction introduces mechanical instabilities that counteract these benefits over time.[44]

To assess whether the pressure-dependent trends persist beyond the initial cycles, we extended galvanostatic cycling to ~100 cycles for cells fabricated at 300 and 500 MPa ((Fig. 4g) and SI sections V and VI). Over this duration, the 500 MPa condition consistently exhibited improved capacity retention relative to 300 MPa (*i.e.*, the capacity decay at 300 MPa was more pronounced). In contrast, cells fabricated at 700 MPa showed rapid degradation and could not be reliably cycled beyond ~10 cycles, indicating premature failure under the highest fabrication pressure.

4 Discussion

The mechanical degradation of secondary NMC532 and NMC811 particles during electrochemical cycling is a complex process, governed by a combination of microstructural evolution, environment-dependent conditions, and processing parameters. The comprehensive experimental and simulation approach presented in this study reveals critical insights into how these factors interplay, affecting both mechanical integrity and electrochemical performance.

Single-particle cycling in the liquid electrolyte shows that capacity degradation is most pronounced after the first charge, with subsequent cycling leading to progressive but less drastic declines. This behavior is strongly linked to the mechanical degradation pathways identified through nanoindentation tests and SEM analysis. The pristine NMC particles initially exhibit a robust and defect-free microstructure, but this integrity is quickly compromised upon charging. The process of delithiation during charging induces lattice contraction, generating internal stresses that promote intergranular cracking, particularly at grain boundaries. Interestingly, after a full charge–discharge cycle, the mechanical response partially recovers, suggesting that lithiation during discharge alleviates some internal stress by allowing the particle to re-expand. However, this recovery is only temporary, as extended cycling leads to irreversible structural damage, with cumulative crack propagation and loss of mechanical integrity. These results emphasize that early-cycle electrochemical state changes are critical for establishing particle-scale damage that persists and evolves with cycling.

The nanoindentation experiments, coupled with DEM simulations, provided an understanding of this degradation. The simulation results, validated by experimental load–displa-

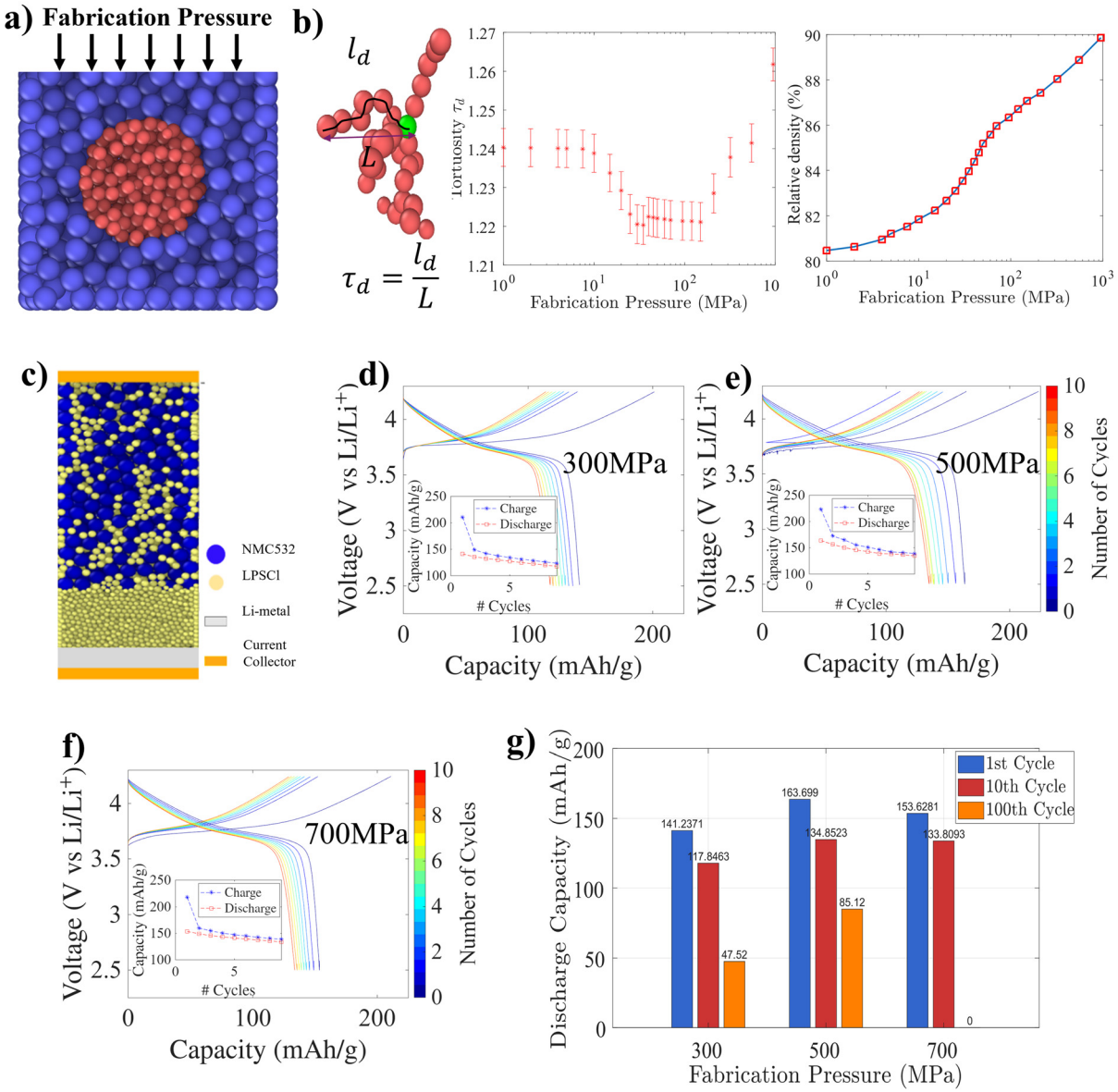

Fig. 4 Solid-state batteries: (a) DEM simulation of a secondary NMC particle assembled at different fabrication pressures; (b) tortuosity evolution as a function of the fabrication pressure and relative density as a function of the fabrication pressure; (c) assembling of full cells fabricated at 300 MPa, 500 MPa, and 700 MPa; (d) voltage *vs.* capacity for the cell fabricated at 300 MPa (inset: temporal evolution of specific capacity over 10 cycles); (e) voltage *vs.* capacity for the cell fabricated at 500 MPa (inset: temporal evolution of specific capacity over 10 cycles); (f) voltage *vs.* capacity for the cell fabricated at 700 MPa (inset: temporal evolution of specific capacity over 10 cycles); and (g) discharge capacity evolution as a function of the fabrication pressure.

cement curves, confirmed that the weakening of intergranular cohesive forces is a critical factor driving mechanical failure. The strong agreement between experiments and simulations emphasizes the predictive power of the DEM model in capturing how crack initiation and propagation evolve under mechanical stress. The DEM results provide a mechanistic bridge between environment-dependent damage evolution (liquid *vs.* solid-contact environments) and the experimentally observed capacity trends by tracking how microcracking/fragmentation accumulates and degrades effective transport pathways and interfacial/contact integrity; here, DEM "cycles" represent repeated loading events rather than a one-to-one mapping to electrochemical cycles. In particular, the simulations also highlighted the role of grain boundary adhesion: once cohesive bonds are compromised, cracks spread rapidly, resulting in secondary particle fracture. Moreover, the ability of the DEM model to replicate fracture behavior across different cycling stages offers a reliable framework for predicting how structural changes influence long-term particle stability.

The influence of the surrounding environment on mechanical degradation was also pronounced. In liquid environments, fluid flow within the interstitial spaces of the particle accelerates crack propagation and structural weakening. Our CFD-DEM simulations revealed that continuous fluid-induced stresses exacerbate mechanical fatigue, leading to a progressive decline in fracture stress over extended cycling. These results emphasize that fluid-induced mechanical stresses are a critical degradation mechanism in liquid systems, reinforcing the need for particle designs that minimize fluid interaction and stress accumulation.

Because the liquid-environment measurements are performed at the single-particle scale while the solid-environment results are obtained in composite full cells, our liquid–solid evaluation is intended to be mechanistic (particle-level damage modes and susceptibility) rather than a one-to-one quantitative comparison of absolute cell performance.

In solid-state environments, the degradation pathway is notably different. The solid-contact matrix imposes confinement on the NMC particles, which can restrict expansion and mitigate some crack propagation. However, this confinement also introduces localized stress concentrations, particularly during cycling and fabrication. The relationship between fabrication pressure and microstructural integrity has emerged as a crucial factor in determining long-term performance. Taken together, the single-particle fracture results quantify a particle-intrinsic 'damage susceptibility' that can be translated into full-cell degradation through (i) loss of electronic percolation within/between fragmented secondary particles, (ii) increased ionic transport resistance (higher tortuosity/lower effective diffusivity), and (iii) reduced particle–electrolyte contact that manifests as impedance growth, effects that are especially consequential in solid-state composite cathodes. While higher pressures initially improve particle packing and reduce tortuosity, pressures exceeding 500 MPa lead to particle fracture and increased tortuosity. This increase in tortuosity disrupts ion transport pathways and correlates with a decline in capacity retention. The electrochemical data confirmed that full cells fabricated at higher pressures exhibited poorer cycling stability, a result directly linked to the fragmentation-induced tortuosity increase of secondary NMC particles. This finding highlights the importance of optimizing fabrication conditions for maintaining ionic conductivity and mechanical integrity.

Notably, chemical interfacial degradation and interphase formation at the NMC–Li_6PS_5Cl interfaces are widely reported and can co-exist with mechanical damage, contributing to impedance growth and capacity fade. In our pressure-series experiments, however, materials and cycling protocol were held constant, so the systematic differences observed with fabrication pressure are most consistently linked to pressure-modulated microstructural/mechanical evolution. Accordingly, while interfacial reactions cannot be ruled out, they are not expected to be the primary origin of the systematic, pressure-dependent trends observed here.[45] Instead, the relative differences with fabrication pressure are most consistently attributed to pressure-modulated microstructural and mechanical factors—such as particle fracture/fragmentation, evolution of particle–electrolyte contact, and changes in effective transport pathways within the composite cathode.

Although the solid environment slowed the rate of degradation compared to the liquid environment, it did not eliminate it. The gradual decline in fracture stress observed over 1000 cycles highlights the persistent influence of mechanical fatigue, even in solid-state configurations. The confinement provided by the solid contact may mitigate large-scale cracking, but repeated volume changes during cycling still induce microstructural damage over time. This observation underscores the need for reinforcement strategies that can better accommodate volume fluctuations, such as the design of more elastic solid electrolyte materials as suggested in the previous work.[46]

Finally, our liquid-*versus*-solid results are intended as a mechanistic contrast using particle-scale damage metrics, rather than a one-to-one system-level comparison of full battery architectures. Overall, the combined experiments and modeling provide design guidance centered on mitigating intergranular damage in secondary NMC: for liquid exposure, reducing crack-assisted penetration and stress accumulation; and for solid-state composite cathodes, optimizing fabrication pressure to balance densification benefits against mechanically driven damage and transport penalties.

5. Conclusions

This study provides a particle-resolved investigation of intergranular mechanical degradation of secondary NMC532 and NMC811 particles in both liquid and solid-state environments, highlighting the critical role of microstructural evolution, electrolyte medium, and fabrication conditions. Through a combination of single-particle electrochemical cycling, nanoindentation experiments, and advanced DEM and CFD-DEM simulations, we identified key degradation mechanisms, including stress-induced intergranular cracking, fluid-induced mechanical fatigue, and pressure-induced particle fracture. In liquid environments, fluid infiltration accelerated crack propagation. In solid-state systems, while confinement slowed degradation, excessive fabrication pressures introduced increased tortuosity and structural damage, negatively impacting ionic transport and capacity retention. These findings underscore the need for tailored strategies, such as controlling fabrication pressure, to enhance the mechanical resilience and long-term performance of cathode materials. The validated simulation framework further offers a powerful predictive tool for future material design and optimization. Importantly, the comparison of liquid *versus* solid environments presented here is intended as a contrast using particle-scale damage metrics, rather than a one-to-one system-level comparison of full battery architectures. Overall, the combined experiments and modeling provide actionable guidance for mitigating intergranular degradation through particle design and processing control,

particularly in pressure-sensitive solid-state composite cathodes.

Author contributions

Fernando David Cúñez: conceptualization, data curation, formal analysis, investigation, methodology, software, validation, and writing – original draft. Radwa Elawadly: formal analysis, investigation, validation, and writing – review & editing. Eric Hintsala: data curation, methodology, and visualization. Wonjoon Suk: data curation, methodology, and visualization. Yiyang Li: formal analysis, supervision, and writing – reviewing and editing. Qingsong Howard Tu: conceptualization, formal analysis, funding acquisition, project administration, resources, software, supervision, and writing – reviewing and editing.

Conflicts of interest

There are no conflicts to declare.

Data availability

Data for this article, including scripts for numerical simulations, RAW data and videos, and MATLAB scripts for processing data, are available at figshare at https://doi.org/10.6084/m9.figshare.30011344.v1. Other data supporting this article have also been included as part of the supplementary information (SI). Supplementary information is available. See DOI: https://doi.org/10.1039/d6eb00095a.

Acknowledgements

The authors acknowledge the U.S. Army DEVCOM ARL Army Research Office (ARO) Energy Sciences Competency, Advanced Energy Materials Program (Award W911NF2310302). The views and conclusions contained in this document are those of the authors and should not be interpreted as representing the official policies, either expressed or implied, of the U.S. Army or the U.S. Government. The modeling work was performed using computational resources: (1) Bridges-2 at the Pittsburgh Supercomputing Center through allocations MAT220031 and EVE230008 from the Advanced Cyberinfrastructure Coordination Ecosystem: Services & Support (ACCESS) program, which is supported by National Science Foundation grants #2138259, #2138286, #2138307, #2137603, and #2138296, and (2) the Department of Energy's Office of Energy Efficiency and Renewable Energy located at the National Renewable Energy Laboratory.

References

1 X. Cai, Y. Yue, Z. Yi, J. Liu, Y. Sheng and Y. Lu, *Nano Energy*, 2024, 110052.
2 B. Nie, Y. Dong and L. Chang, *J. Energy Storage*, 2024, **96**, 112624.
3 P. M. Roy, H. H. Sawant, P. P. Shelar, P. U. Sarode and S. Gawande, *Energy Storage Sav.*, 2024, **3**, 190–208.
4 H. Xu, Y. Su, C. Zheng, Y. Wang, Y. Tong, Z. Yang and J. Hu, *Chin. Chem. Lett.*, 2024, **35**, 109173.
5 M. M. Thackeray, C. Wolverton and E. D. Isaacs, *Energy Environ. Sci.*, 2012, **5**, 7854–7863.
6 M. Armand and J.-M. Tarascon, *Nature*, 2008, **451**, 652–657.
7 J. Chen, J. Wu, X. Wang, A. Zhou and Z. Yang, *Energy Storage Mater.*, 2021, **35**, 70–87.
8 J. Janek and W. G. Zeier, *Nat. Energy*, 2016, **1**, 16141.
9 Z. Zeng, J. Cheng, Y. Li, H. Zhang, D. Li, H. Liu, F. Ji, Q. Sun and L. Ci, *Mater. Today Phys.*, 2023, **32**, 101009.
10 T. Shi, Q. Tu, Y. Tian, Y. Xiao, L. J. Miara, O. Kononova and G. Ceder, *Adv. Energy Mater.*, 2020, **10**, 1902881.
11 F. Strauss, T. Bartsch, L. De Biasi, A. Y. Kim, J. Janek, P. Hartmann and T. Brezesinski, *ACS Energy Lett.*, 2018, **3**, 992–996.
12 L. Wheatcroft, A. Bird, N. Gollapally, S. G. Booth, S. A. Cussen and B. J. Inkson, *Batteries Supercaps*, 2024, **7**, e202400077.
13 C. Liu, F. Roters and D. Raabe, *Nat. Commun.*, 2024, **15**, 1–18.
14 S. Kalnaus, N. J. Dudney, A. S. Westover, E. Herbert and S. Hackney, *Science*, 2023, **381**, eabg5998.
15 W. Shen, K. Li, J. Huang, X. Qu, X. Chen, G. Fu, Y. Li, Y. Zhang and Y. Lin, *ACS Appl. Energy Mater.*, 2024, **7**, 6384–6399.
16 C. Wang, R. Yu, S. Hwang, J. Liang, X. Li, C. Zhao, Y. Sun, J. Wang, N. Holmes, R. Li, H. Huang, S. Zhao, L. Zhang, S. Lu, D. Su and X. Sun, *Energy Storage Mater.*, 2020, **30**, 98–103.
17 J. Min, W. Suk, S. C. Y. Wong and Y. Li, *Adv. Funct. Mater.*, 2024, **34**, 2410241.
18 K. Raju, L. Wheatcroft, M. C. Lai, A. Mahadevegowda, L. F. J. Piper, C. Ducati, B. J. Inkson and M. De Volder, *J. Electrochem. Soc.*, 2024, **171**, 080519.
19 D. Dang, Y. Wang and Y.-T. Cheng, *J. Electrochem. Soc.*, 2019, **166**, A2749–A2751.
20 W. Jiang, X. Zhu, R. Huang, S. Zhao, X. Fan, M. Ling, C. Liang and L. Wang, *Adv. Energy Mater.*, 2022, **12**, 2103473.
21 Y. Tang, Z. Huang, W. Wang, Y. Wen, S. Zhang, X. Chen, Z. Zhang, Z. Yin, T. Yang, T. Li, L. C. Gallington, H. Zhu, S. Lan, S. Wang, Y. Ren, Z. Wu and Q. Liu, *Nano Energy*, 2024, **128**, 109908.
22 K. Mao, Y. Yao, Y. Chen, W. Li, X. Shen, J. Song, H. Chen, W. Luan and K. Wu, *J. Energy Storage*, 2024, **84**, 110807.

23 M. H. Jeong, J. Kim, D. W. Ham, J. Kim, I. Phiri and S. Y. Ryou, *J. Ind. Eng. Chem.*, 2025, **143**, 410–415.
24 C.-H. Jung, H. Shim, D. Eum and S.-H. Hong, *J. Korean Ceram. Soc.*, 2021, **58**, 1–27.
25 I. Cho, J. Choi, K. Kim, M.-H. Ryou and Y. M. Lee, *RSC Adv.*, 2015, **5**, 95073–95078.
26 L. Britala, M. Marinaro and G. Kucinskis, *J. Energy Storage*, 2023, **73**, 108875.
27 C. H. Lee, B. Jun, S. C. Lee and S. U. Lee, *Mater. Adv.*, 2021, **2**, 3965–3970.
28 Y.-k. Ahn, Y. N. Jo, W. Cho, J.-S. Yu and K. J. Kim, *Energies*, 2019, **12**, 1638.
29 I. Buchberger, S. Seidlmayer, A. Pokharel, M. Piana, J. Hattendorff, P. Kudejova, R. Gilles and H. A. Gasteiger, *J. Electrochem. Soc.*, 2015, **162**, A2737.
30 S. Klein, P. Bärmann, T. Beuse, K. Borzutzki, J. E. Frerichs, J. Kasnatscheew, M. Winter and T. Placke, *ChemSusChem*, 2021, **14**, 595–613.
31 F. D. Cúñez, R. Elawadly, J. Vazquez and Q. H. Tu, *J. Energy Storage*, 2025, **136**, 118412.
32 P. C. Tsai, B. Wen, M. Wolfman, M. J. Choe, M. S. Pan, L. Su, K. Thornton, J. Cabana and Y. M. Chiang, *Energy Environ. Sci.*, 2018, **11**, 860–871.
33 R. Ruess, S. Schweidler, H. Hemmelmann, G. Conforto, A. Bielefeld, D. A. Weber, J. Sann, M. T. Elm and J. Janek, *J. Electrochem. Soc.*, 2020, **167**, 100532.
34 L. Wheatcroft, A. Bird, J. C. Stallard, R. L. Mitchell, S. G. Booth, A. J. Nedoma, M. F. L. De Volder, S. A. Cussen, N. A. Fleck and B. J. Inkson, *Batteries Supercaps*, 2023, **6**, e202300032.
35 Y. Li, Y. Cho, J. Cai, C. Kim, X. Zheng, W. Wu, A. L. Musgrove, Y. Su, R. L. Sacci, Z. Chen, *et al.*, *Mater. Horiz.*, 2025, **12**, 119–130.
36 X. Hu, Z. Zhao, Y. Zhao, X. Wang, S. Sainio, D. Nordlund, C. M. Ruse, X.-D. Zhou, S. W. Boettcher, D. Hou, *et al.*, *J. Mater. Chem. A*, 2024, **12**, 3700–3710.
37 P. Naillou, A. Boulineau, E. De Vito, E. Lavanant and P. Azaïs, *Energy Storage Mater.*, 2025, **75**, 104050.
38 W. Suk, J. Min, T. Liu and Y. Li, *Chem. Mater.*, 2025, **37**, 1788–1797.
39 Y. Hiramatsu and Y. Oka, *International Journal of Rock Mechanics and Mining Sciences & Geomechanics Abstracts*, 1966, pp. 89–90.
40 G. Žagar, V. Pejchal, M. Kissling and A. Mortensen, *Eur. J. Mech. A/Solids*, 2018, **72**, 148–154.
41 C. Kloss, C. Goniva, A. Hager, S. Amberger and S. Pirker, *Prog. Comput. Fluid Dyn.*, 2012, **12**, 140–152.
42 C. Lischka and H. Nirschl, *Energy Technol.*, 2023, **11**, 2200849.
43 T.-N. Kröger, P. Harte, S. Klein, T. Beuse, M. Börner, M. Winter, S. Nowak and S. Wiemers-Meyer, *J. Power Sources*, 2022, **527**, 231204.
44 I. A. Shozib, F. D. Cúñez, M. Ganter, A. Leggiero, R. Liu and Q. H. Tu, *J. Electrochem. Soc.*, 2024, **171**, 090524.
45 M. S. Diallo, T. Shi, Y. Zhang, X. Peng, I. Shozib, Y. Wang, L. J. Miara, M. C. Scott, Q. H. Tu and G. Ceder, *Nat. Commun.*, 2024, **15**, 858.
46 S. Farzanian, J. Vazquez Mercado, I. Shozib, N. Sivadas, V. Lacivita, Y. Wang and Q. H. Tu, *ACS Appl. Energy Mater.*, 2023, **6**, 9615–9623.